MECSOL 2019 - Proceedings of the 7th International Symposium on Solid Mechanics,
V. Tita, A. Ferreira, M.L. Ribeiro, A. Vieira and A.T. Beck (Editors), ABCM, Sao Carlos, SP, Brazil, April 15th to 17th, 2019

An Energy Based Failure Model to Predict the Crushing Behavior of Unidirectional Composite Laminates

Sérgio Augusto Capasciutti de Oliveira , Maurício Vicente Donadon

Instituto Tecnológico de Aeronáutica – ITA – IEA – Praça Marechal Eduardo Gomes, 50, São José dos Campos – SP, 12228-900, Brazil. scapas@ita.br/donadon@ita.br

Abstract: Crashworthiness is an application of crushing loads in structures, where energy of crash shall be absorbed through the failure mechanisms of the material used in such structures. In the case of composites, few failure mechanisms shall be taken into account in order to propose a computational failure damage based on energy balance to comply with the physical problem. In this work, a continuum damage mechanics based failure model is proposed to predict the crushing behavior of UD composite laminates. The model enables prediction typical failure mechanisms commonly observed in UD laminates under crush loading with high-fidelity by incorporating into its formulation a set of phenomenological stress-based criteria to detect damage initiation and fracture mechanics combined with an element deletion strategy to predict damage progression. A VUMAT subroutine was implemented into ABAQUS/Explicit finite element model (FEM) to access the problem through the investigation of unidirectional carbon/epoxy laminates with wedge shaped tip triggers.

Keywords: crashworthiness, energy, crushing, failure, impact

INTRODUCTION

Crashworthiness plays an important role into the rule books of passenger vehicles as cars, aircrafts and rotorcrafts, and in the motorsport environment (De Oliveira and Donadon, 2017). In the Fig. 1(a) and Fig. 1(b) Bisagni et al. (2005) and Heimbs et al. (2009) depicted some components of a Formula 1 (F1) that car shall comply with the FIA regarding crashworthiness requirements in order to compete in the world championship. Expensive FIA crash tests shall be provided by the F1 constructors to validate the frontal, rear and side impact, and also, steering wheel column attenuators in terms of crashworthiness requirements. To save costs, a considerable effort has been dedicated by the F1 teams towards the development of a FE based virtual testing platform to simulate the crashworthiness event.

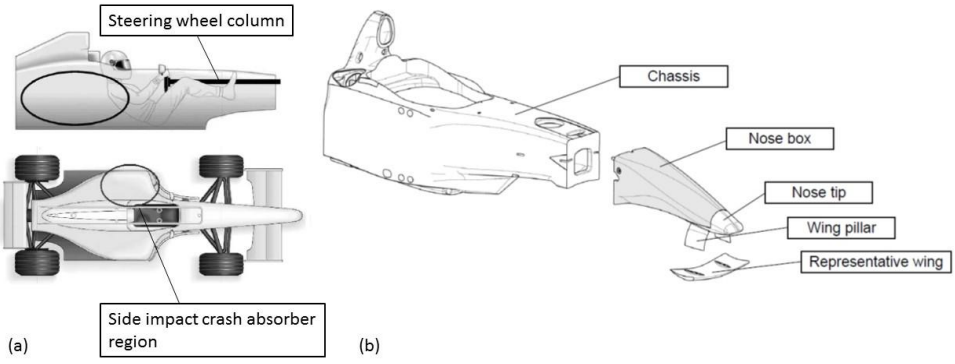

Figure 1 – (a) Steering wheel column and side impact crash absorber. (Bisagni et al. 2005). (b) Frontal impact crash absorber. (Heimbs et al. 2009).

Within this context, this work presents recent advances on the formulation and implementation of high-fidelity finite element models to predict the crushing response of the aforementioned structures when subjected to the FIA requirements. The models presented herein will integrate the virtual testing platform for composite structures under development in the Laboratory of New Concepts in Aeronautics (LNCA) at ITA.

DAMAGE MODEL

The proposed damage model is based on the Continuum Damage Mechanics (CDM) and implemented into VUMAT ABAQUS/Explicit user defined material subroutine, where the damage evolution laws enables to predict each of the five failure modes investigated here for the intralaminar domain within an energy based framework:

- fiber in tension;
- fiber in compression;
- matrix in tension;
- matrix in compression;
- in-plane shear.

Intralaminar Damage Model

The intralaminar failure model used herein accounts for the five modes aforementioned, and its formulation is based on a set of criteria to be predict failure initiation, damage propagation and element deletion strategy at ply level. This model was first proposed by Donadon et al. (2009).

Criteria for Fiber Failure Initiation in Tension and Compression

The failure criteria, F_1^t for fiber failure in tension and F_1^c for fiber failure in compression are based on maximum stress, where the local stress-strain relationship is defined in terms of the softening law shown in Fig. 2.

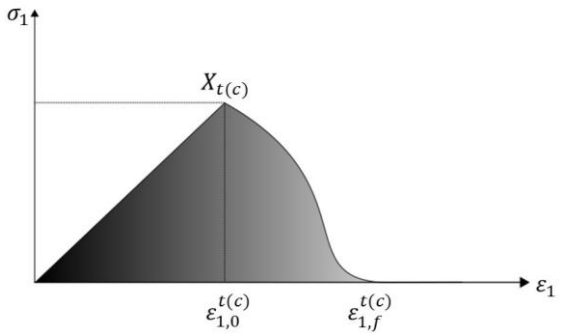

Figure 2 – Stress-strain softening law for fiber failure modes

Where to the local tensile or compression stress σ_1 is compared with the fiber strength in tension and compression ($X_{t(c)}$). The subscripts in $X_{t(c)}$ means tension (t) and compression (c). The same designation is used for the strains superscripts $\varepsilon_{1,0}^{t(c)}$ and $\varepsilon_{1,f}^{t(c)}$. Maximum stress in the fiber direction for tension and compression modes is given by Equations (1) and (2), respectively. $\varepsilon_{1,0}^{t(c)}$ is the onset failure strain for tension or compression failure modes also, while $\varepsilon_{1,f}^{t(c)}$ is the final strain, considering that the material is not able to carry more load.

$$F_1^t\left(\sigma_1\right)=\frac{\sigma_1}{X_t}\geq 1.0 \tag{1}$$

$$F_1^c\left(\sigma_1\right)=\frac{\left|\sigma_1\right|}{X_c}\geq 1.0 \tag{2}$$

Damage Evolution Laws for Fiber in Tension and Compression

Once the failure initiation has been detected according to Equations (1) and (2), the damage evolution laws are given by Equations (3) and (5) respectively for fiber failure in tension and compression.

$$d_1^t\left(\varepsilon_1^+\right)=1-\frac{\varepsilon_{1,0}^t}{\varepsilon_1^+}\left[1+\kappa_{1,t}^2\left(\varepsilon_1^+\right)\left(2\kappa_{1,t}\left(\varepsilon_1^+\right)-3\right)\right] \tag{3}$$

Where,

$$\kappa_{1,t}\left(\varepsilon_1^+\right)=\frac{\varepsilon_1^+-\varepsilon_{1,0}^t}{\varepsilon_{1,f}^t-\varepsilon_{1,0}^t} \tag{4}$$

$$d_1^c\left(\varepsilon_1^-\right)=1-\frac{\varepsilon_{1,0}^c}{\varepsilon_1^-}\left[1+\kappa_{1,c}^2\left(\varepsilon_1^-\right)\left(2\kappa_{1,c}\left(\varepsilon_1^-\right)-3\right)\right] \tag{5}$$

With,

$$\kappa_{1,c}\left(\varepsilon_1^-\right)=\frac{\varepsilon_1^--\varepsilon_{1,0}^c}{\varepsilon_{1,f}^c-\varepsilon_{1,0}^c} \tag{6}$$

The strains ε_1^+ and ε_1^- are the maximum strains in tension and compression, respectively, achieved in time *t*, even if the respective onset fiber damage has been triggered. The final strains in Equations (3)-(6) and depicted in Fig. 2 are given by Equations (7) and (8):

$$\varepsilon_{1,f}^t=\frac{2G_{fiber}^t}{X_t l_1^t} \tag{7}$$

$$\varepsilon_{1,f}^c=\frac{2G_{fiber}^c}{X_c l_1^c} \tag{8}$$

Where , G_{fiber}^t , G_{fiber}^c , l_1^t and l_1^c are the fracture toughness for the fiber failure in tension, fracture toughness for the fiber failure in compression, the characteristic lengths of the element in tension and compression, respectively.

Criteria for Matrix Cracking Initiation in Tension and Compression

In the case of the failure of the matrix in tension (F_2^t) and compression (F_2^c), the criteria are given by Equation (9) and (10). In matrix failure, under tensile stress, the Hashin criterion was implemented in the VUMAT constitutive model subroutine, while for matrix subjected to compression load, Puck and Schürmann was used. As aforementioned described in the fiber failure modes, the two failure criteria presented in Equations (9) and (10) follow a similar softening law based on the stress-strain relationship, depicted in Fig. 3.

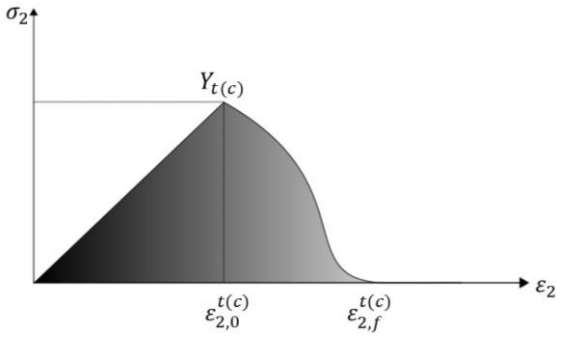

Figure 3 – Stress-strain softening law for matrix dominated failure modes

In Fig. 3, $Y_{t(c)}$, $\varepsilon_{2,0}^{t(c)}$ and $\varepsilon_{2,f}^{t(c)}$ are the matrix strengths in tension and compression (subscripts defined above), matrix onset failure for tension and compression and final strain when the element is no longer capable of carrying additional load, respectively.

$$F_2^t\left(\sigma_2,\tau_{23},\tau_{12}\right)=\left(\frac{\sigma_2}{Y_t}\right)^2+\left(\frac{\tau_{23}}{S_{23}}\right)^2+\left(\frac{\tau_{12}}{S_{12}}\right)^2\geq 1.0 \tag{9}$$

The mechanical properties S_{12} and S_{23} are the local shear strengths in the planes *12* and *23*, respectively.

$$F_2^c\left(\sigma_{nt},\sigma_{nl}\right)=\left(\frac{\sigma_{nt}}{S_{23}^A-\mu_{nt}\sigma_{nn}}\right)^2+\left(\frac{\sigma_{nl}}{S_{12}-\mu_{nl}\sigma_{nn}}\right)^2\geq 1.0 \tag{10}$$

Where the stress σ_{nn}, σ_{nl} and σ_{nt} comes from the potential fracture plane defined by the criterion. (Donadon et al. 2009).

The local stress (σ_{fp}) and the strains (ε_{fp}) in the potential fracture plane, comes:

$$\sigma_{fp}=[T][\sigma_{123}][T]^T=\begin{bmatrix}\sigma_{11} & \tau_{nt} & \tau_{lt}\\ \tau_{nt} & \sigma_{nn} & \tau_{nl}\\ \tau_{lt} & \tau_{nl} & \sigma_{tt}\end{bmatrix} \tag{11}$$

$$\varepsilon_{fp}=[T][\varepsilon_{123}][T]^T=\begin{bmatrix}\varepsilon_{11} & \varepsilon_{nt} & \varepsilon_{lt}\\ \varepsilon_{nt} & \varepsilon_{nn} & \varepsilon_{nl}\\ \varepsilon_{lt} & \varepsilon_{nl} & \varepsilon_{tt}\end{bmatrix} \tag{12}$$

Where $[T]$ is coordinates transformation matrix given by Equation (13), σ_{123} is the material coordinate stress tensor at ply level, given by Equation (14) and ε_{123} is the material coordinates strain tensor, according to Equation (15).

$$[T]=\begin{bmatrix}1 & 0 & 0\\ 0 & \cos(\theta) & -\sin(\theta)\\ 0 & \sin(\theta) & \cos(\theta)\end{bmatrix} \tag{13}$$

$$[\sigma_{123}]=\begin{bmatrix}\sigma_{11} & \tau_{12} & \tau_{13}\\ \tau_{12} & \sigma_{22} & \tau_{23}\\ \tau_{13} & \tau_{23} & \sigma_{33}\end{bmatrix} \tag{14}$$

$$[\varepsilon_{123}]=\begin{bmatrix}\varepsilon_{11} & \varepsilon_{12} & \varepsilon_{13}\\ \varepsilon_{12} & \varepsilon_{22} & \varepsilon_{23}\\ \varepsilon_{13} & \varepsilon_{23} & \varepsilon_{33}\end{bmatrix} \tag{15}$$

Damage Evolution Laws for Matrix Cracking in Tension and Compression

The damage evolution law for the matrix in tension is given by Equation (16):

$$d_m^t\left(\bar{\varepsilon}_{m,0}^{t}\right)=1-\frac{\varepsilon_{m,0}^t}{\bar{\varepsilon}_m^t}\left[1+\kappa_{m,t}^2\left(\bar{\varepsilon}_m^t\right)\left(2\kappa_{m,t}\left(\bar{\varepsilon}_m^t\right)-3\right)\right] \tag{16}$$

$$\kappa_{m,t}(\bar{\varepsilon}_m^t)=\frac{\bar{\varepsilon}_m^t-\bar{\varepsilon}_{m,0}^t}{\bar{\varepsilon}_{m,f}^t-\bar{\varepsilon}_{m,0}^t} \tag{17}$$

Where $\bar{\varepsilon}_m^t$ is the resultant strain given by Equation (18). $\bar{\varepsilon}_{m,0}^t$ is the damage onset resultant strain.

$$\bar{\varepsilon}_m^t=\sqrt{\varepsilon_2^2+\gamma_{s,m}^2} \tag{18}$$

$$\bar{\gamma}_{s,m} = \sqrt{\gamma_{12}^2 + \gamma_{23}^2} \tag{19}$$

And $\bar{\varepsilon}_{m,f}^{t}$ is the resultant final strain for the matrix in tension, given by Equation (20) below.

$$\bar{\varepsilon}_{m,f}^{t} = \frac{2}{\bar{\sigma}_{m,0}^{t}} \left[\left(\frac{\cos^2(\theta)}{g_{mc}^{t}} \right)^{\lambda} + \left(\frac{\sin^2(\theta)}{g_{mc}^{s}} \right)^{\lambda} \right]^{-1/\lambda} \tag{20}$$

With $g_{mc}^{t} = G_{matrix}^{t} / l_2^{t}$ and $g_{mc}^{s} = G_{shear} / l_2^{t}$. Where l_2^{t} and G_{shear} are the characteristic length of the element in the beginning of the simulation.

$$d_m^c\left(\bar{\varepsilon}_{m,0}^{c}\right) = 1 - \frac{\bar{\varepsilon}_{m,0}^{c}}{\bar{\varepsilon}_{m}^{t}} \left[1 + \kappa_{m,c}^2\left(\bar{\varepsilon}_{m}^{c}\right)\left(2\kappa_{m,c}\left(\bar{\varepsilon}_{m}^{c}\right) - 3\right) \right] \tag{21}$$

$$\kappa_{m,c}(\bar{\varepsilon}_{m}^{c}) = \frac{\bar{\varepsilon}_{m}^{c} - \bar{\varepsilon}_{m,0}^{c}}{\bar{\varepsilon}_{m,f}^{c} - \bar{\varepsilon}_{m,0}^{c}} \tag{22}$$

Where $\bar{\varepsilon}_{m}^{c}$ is the resultant shear strain on the Puck and Schürmann formulation action plane. And $\bar{\varepsilon}_{m,0}^{c}$ is the onset damage resultant strain for the compression stress in the transverse (matrix) direction.

$$\bar{\varepsilon}_{m}^{c} = \sqrt{\varepsilon_{nl}^2 + \varepsilon_{nt}^2} \tag{23}$$

$$\bar{\varepsilon}_{m,f}^{c} = \frac{2G_{matrix}^{c}}{\bar{\sigma}_{m,0}^{c} l_2^{c}} \tag{24}$$

In Equation (24), G_{matrix}^{c} and l_2^{c} are the toughness for matrix cracking in compression and the characteristic length of the element associated with the matrix cracking in compression, respectively.

Criterion for In-Plane Shear Failure Initiation

The failure criterion, for in-plane shear is, F_{12} and is given by the Equation (25) below. As the other failure modes, in-plane shear is based on the stress-strain relationship shown in Fig. 4.

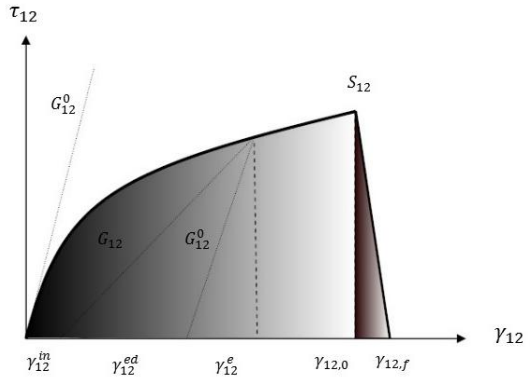

Figure 4 – Stress-strain curve for in-plane shear failure mode

$$F_{12}\left(\tau_{12}\right) = \frac{\left|\tau_{12}\right|}{S_{12}} \geq 1.0 \tag{25}$$

Damage Evolution Law for In-Plane Shear

$$d_{12}\left(\gamma_{12}\right) = 1 - \frac{\gamma_{12,0} - \gamma_{12,0}^{i}}{\gamma_{12} - \gamma_{12,0}^{i}} \left[1 + \kappa_{12}^2\left(\gamma_{12}\right)\left(2\kappa_{12}\left(\gamma_{12}\right) - 3\right) \right] \tag{26}$$

Where γ_{12}^{i}, γ_{12}^{e} in Fig. 4 are the inelastic and elastic shear strain, respectively. The total strain can be decomposed into elastic strain and damage strain, according to Equation (27).

$$\gamma_{12} = \gamma_{12}^{e} + \gamma_{12}^{d} \tag{27}$$

And the elastic-damage strain in Fig. 4, can be defined as:

$$\gamma_{12}^{ed} = \gamma_{12}^{in} - \gamma_{12}^{d} \tag{28}$$

$$\kappa_{12}(\gamma_{12}) = \frac{\gamma_{12} - \gamma_{12,0} - 2\gamma_{12,0}^{i}}{\gamma_{12,0} - \gamma_{12,0}^{i} - \gamma_{12,f}} \tag{29}$$

Where $\gamma_{12,0}$ and $\gamma_{12,0}^{i}$ are the current strain and the total inelastic strain at failure, when $\tau_{12} = S_{12}$ in Fig. 4.

And the final strain for the in-plane shear failure mode is given by Equation (30).

$$\gamma_{12,f} = \frac{2G_{shear}}{S_{12} l_{12}} \tag{30}$$

Where G_{shear} and l_{12} are the in-plane shear failure toughness and the characteristic length of the element associated with the matrix cracking in shear, respectively.

Interlaminar Damage Model

The in-built cohesive laws available in ABAQUS/Explicit were used to model the cohesive 3D interface, with COH3D8 elements between plies, with an interply cohesive domain with 10% of each ply thickness. The interlaminar damage initiation detection is based on the maximum stress criterion and damage propagation is based on an energy-based linear traction-separation softening law whose final displacement associated with the elemental fully failed behavior is determined based on the *B-K* mixed mode formulation. The mechanical properties used for the cohesive 3D interface element are given on Tab. A.1.

FINITE ELEMENT MODEL

Two finite element simulation was carried out in ABAQUS/Explicit, (Specimen A and Specimen B) using the dimensions proposed by Tan et al. (2015), also based in the work of Israr et al. (2013) and Israr et al (2014). According to Figure 5, the height of the wedge shaped tip plate is 35.0 *mm* in total, with the unclamped part of the specimen is 30.0 *mm* high and was meshed with C3D8R reduced integration available in ABAQUS/Explicit, with element size of 0.25 x 0.25 *mm*. In order to reduce the simulation time only half of the specimen was modelled with symmetry boundary conditions in the plane normal to *Z* direction and the crushing plate was modelled as analytic rigid. The contact algorithm used between the analytic rigid plate and the wedge shaped tip plate was general contact with "hard" normal behavior and tangential behavior with a penalty of 0.2 for friction coefficient. Elements are deleted when $d = \max[d_1^t(\varepsilon_1), d_1^c(\varepsilon_1)]$ is equal to 1.0 or the determinant of the gradient deformation are between 0.8 and 1.6. The mechanical properties of each ply are listed on Tab. A.2 and Tab. A.3.

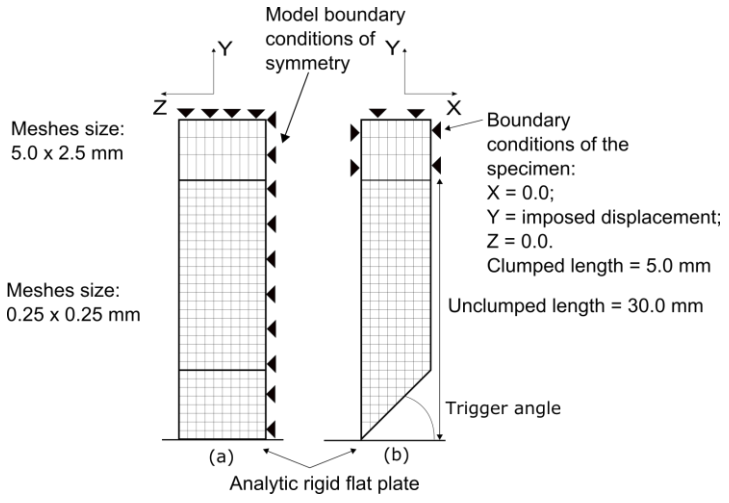

Figure 5 – (a) Front view of the finite element model. (b) Side view of the finite element model

On Tab. 1 and on Fig. 5 (a) and (b), the dimensions are given for the two models, Specimen A and Specimen B.

Table 1 – Specimen A and Specimen B dimensions

Specimen	Lay-up	Thickness (*mm*)	Total height (mm)	Width (mm)	Trigger angle (°)
Specimen A	$[(0°/90°)_4]_s$	4.16	35.0	8.32	20
Specimen B	$[(0°/90°)_4]_s$	4.16	35.0	10.0	45

RESULTS

Specimen A

In Fig. 6 is possible to verify the similarity of the crushing morphology regarding the splaying, fragmentation and debris modes of the plies of the Specimen A (20° tip trigger), when compared to the experiments carried out by Israr et al (2013) and the FEM. For the crushing displacement of 0.55, 1.4, 1.6, 3.6, 5.0 and 8.5 *mm* shown in Figure 6, the FEM model morphologies show good correlation with the experiment. The load *versus* displacement curve in Fig. 7(a) indicates an error between the experiment and the model prediction of about 2.2%, in terms of peak load, 5.083*kN* for the experiment and 5.197*kN* for the model. The result presented in Fig. 7(b), indicates that the model over predicts the internal energy absorbed, 17.7*J*, when compared to the experiment, 11.1*J*. However, in terms of overall structural response and damage morphology, it is possible to conclude that the proposed constitutive model implemented in ABAQUS/Explicit FEM can predict with high-fidelity the failure modes and the resultant load of the crushing process of composite unidirectional carbon/epoxy wedge shaped tip trigger plates.

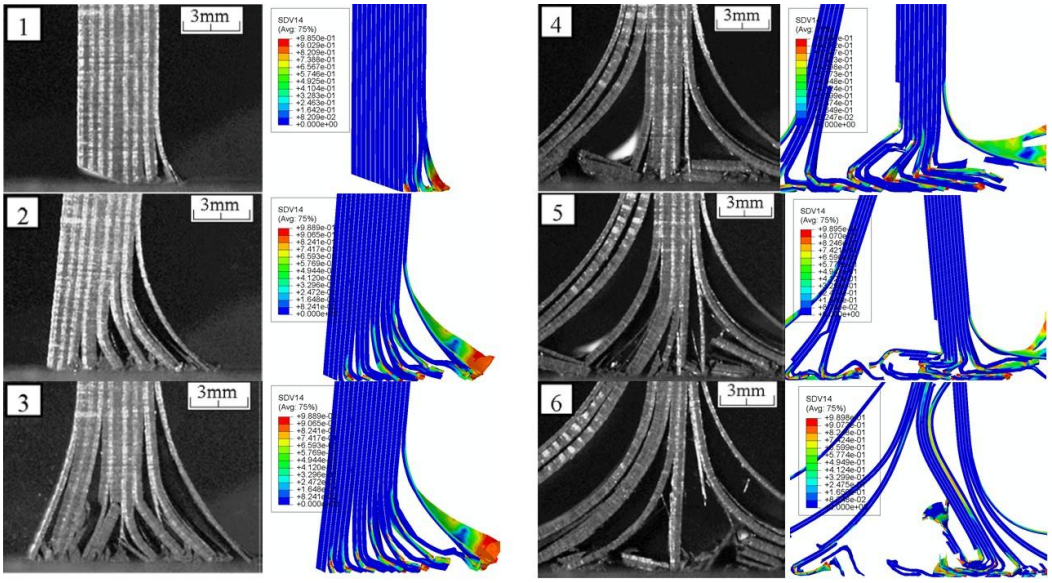

Figure 6 – (a) Experiment (Israr et al. 2013) *versus* FEM model morphologies, for displacements 0.55, 1.4, 1.6, 3.6, 5.0 and 8.5 *mm*.

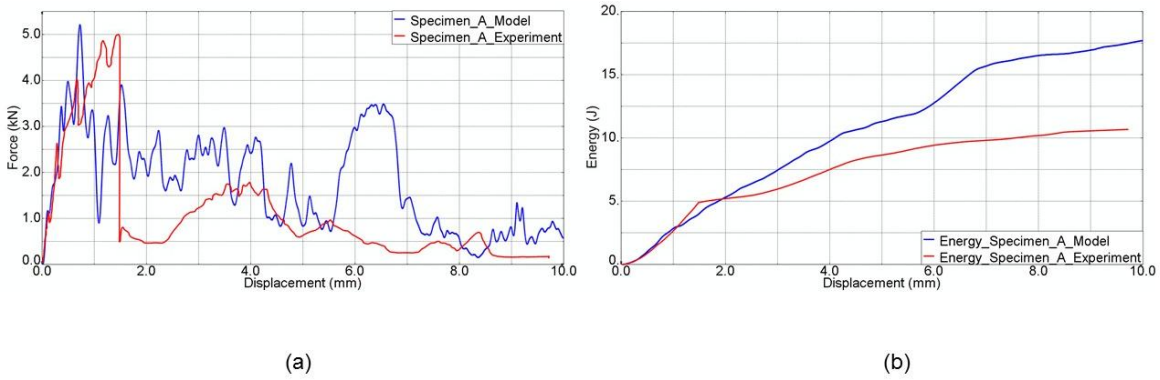

Figure 7 – (a) Experimental (Israr et al. 2013) *versus* FEM model predictions: (a) force *versus* displacement. (b) Internal energy *versus* displacement.

Specimen B

In Fig. 8, the morphology in the experiment (Israr et al. 2014) was compared with numerical predictions using the same parameters. For the displacements of 3.0, 4.0, 6.5 and 9.5 *mm*, the crushing failure mechanisms, as splaying, fragmentation and debris were present in the experiment and in the model. In Fig. 9(a), the load *versus* displacement curve shows the peak load for the experiment I and experiment II, 4.4*kN* and 4.9*kN*, respectively. For specimen B, the predicted peak load was 4.604*kN*. The error between the average peak load of the experiment and the one predicted by the model was 1.0%. Similarly to the previous case, the model also over predicted the absorbed energy compared to the experimental absorbed energy.

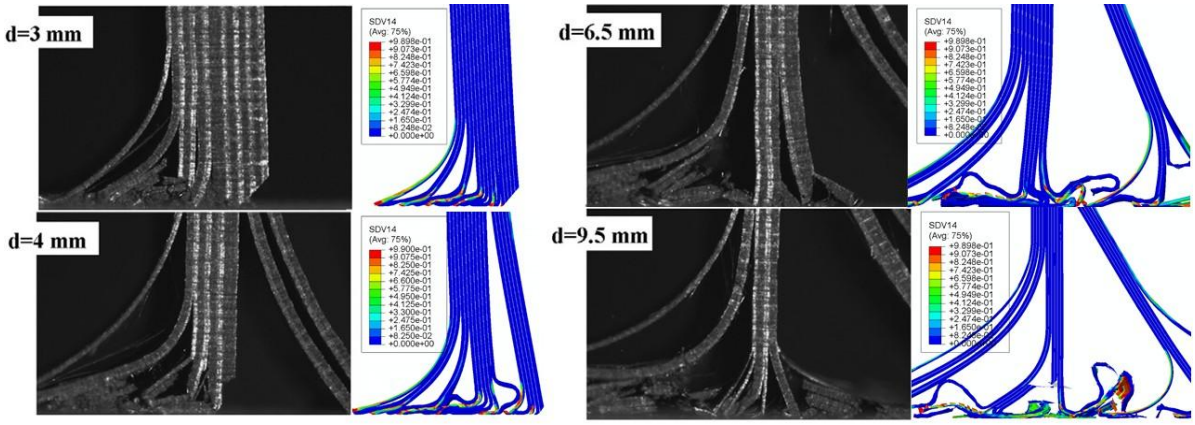

Figure 8 – Experiment (Israr et al. 2014) *versus* FEM model morphology.

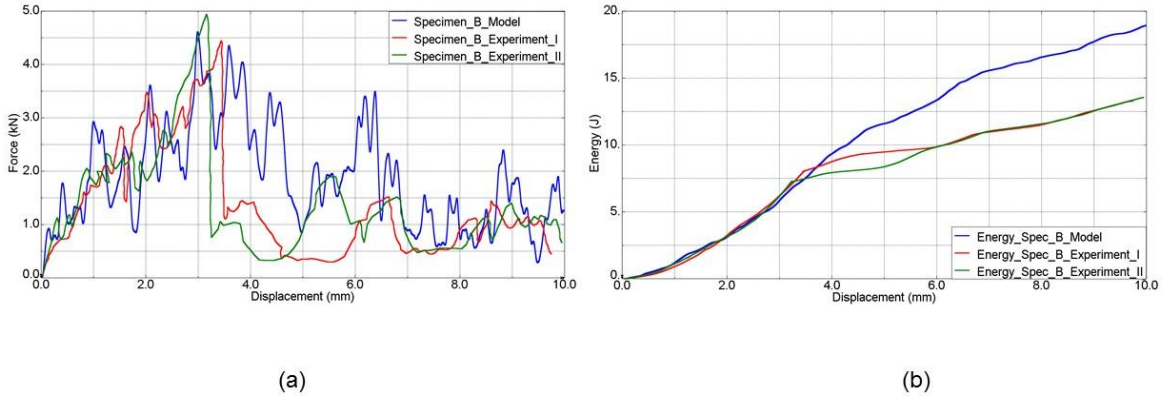

Figure 9 – (a) Experiment (Israr et al. 2013) *versus* FEM model morphologies. (b) Force *versus* Displacement curves – Models and Experiment (Israr et al. 2013)

CONCLUSIONS

In this work, a crashworthiness assessment numerical tool (VUMAT constitutive model plus the ABAQUS/Explicit FEM) is presented to be used in design of structures to absorb crash energies. Although load *versus* displacement curves and internal energy *versus* displacement curves show good correlation with the experiments provided by Israr el al. (2013) and Israr et al. (2014), there are some differences between experimental and numerical values of the internal absorbed energies, for Specimen A and B. These results can be explained by the fact that an extra part of the total energy absorption predicted by the model is numerically dissipated by the hourglass and element distortion control algorithms required by the single integration point elements (C3D8R available in ABAQUS/Explicit) used in the simulations.

The proposed model also provides fairly good prediction in terms of damage morphology commonly observed in composite laminates under crushing load. As depicted in Fig. (6) and in Fig. (8), the crush front morphology shows good correlation with the experimental results available in the open literature.

It is worth to mention that some properties used in the simulations, particularly the intralaminar fracture toughness values, were taken from open literature and extra studies and are underway in order to better understand the effects of these parameters on the overall structure response of the composite laminates simulated herein. Additionally,

experimental tests will be performed at ITA using similar material where these parameters are known. The results obtained from this testing program will be used to provide consistent experimental database for the model validation.

For future works, in order to increase the accuracy of the presented damage model, fiber kinking prediction, replacing the current maximum stress based formulation shall be implemented. Additionally, the strain rate effects will be incorporated into the constitutive model formulation in order to better describe the physics of the impact under different loading regimes.

ACKNOWLEDGMENTS

The authors acknowledge the financial support received for this work from CAPES (Coordination for the Improvement of Higher Level -or Education- Personnel, Finance Code 001), CNPq (National Research Council) Grant 301053/2016-2 and FINEP/CAPTAER II, Grant 0109020700.

REFERENCES

Bisagni, C., Di Pietro, G., Fraschini, L., Terletti, D., 2005, "Progressive Crushing of Fiber-Reinforced Composite Structural Components of a Formula One Racing Car.", Composite Structures, Elsevier, Vol.68, No. 4, pp 491-503.

De Oliveira, S.A.C., Donadon, M.V., 2017, "Predicting Crushing Behavior of Unidirectional Laminates with Wedge Shaped Tip Trigger of 45°." Meeting on Aeronautical Composite Materials and Structures – MACMS 2017.

Donadon, M.V., De Almeida, S.F.M., Arbelo, M.A., De Faria, A.R., 2009, "A Three-Dimensional Ply Failure Model for Composite Structures." , International Journal of Aerospace Engineering, Hindawi Publishing Corporation.

Heimbs, S., Strobl, F., Middendorf, S., Gardner, B., Eddington, B., Key, J., 2009, "Crash Simulation of an F1 Racing Car Front Impact Structure.", 7th European LS-Dyna Conference, DYNAmore GmbH.[S.I.: s.n].

Israr, H.A., Rivallant, S., Barrau, J.J., 2013, "Experimental Investigation on Mean Crushing Stress Characterization of Carbon-Epoxy Plies Under Compressive Crushing Mode." Composite Structures, Elsevier, Vol. 96, pp 357-364.

Israr, H.A., Rivallant, Bouvet, C., S., Barrau, J.J., 2014, "Finite Element Simulation of 0°/90° CFRP laminated plates Subjected to Crushing Using a Free-Face-Crushing Concept." Composites: Part A, Elsevier, Vol. 62, pp 16-25.

Tan, W., Falzon, B.G., Price, M., 2015, "Predicting the Crushing Behaviour of Composite Material Using High-Fidelity Finite Element Modelling." International Journal of Crashworthiness, 20:1, 60-77, DOI: 10-1080/13588265.2014.972122.

RESPONSIBILITY NOTICE

The authors are the only responsible for the printed material included in this paper.

APPENDIX

In this appendix the mechanical properties of the material used in the numerical simulations are presented.

Table A.1 – Interface element mechanical properties

Mechanical Property	Parameter	Value
Interlaminar Fracture Toughness	G_I	0.6×10^3 *N/m*
	G_{II}	2.1×10^3 *N/m*
	G_{III}	2.1×10^3 *N/m*
Strength Properties	N	121.0 *MPa*
	S_{13}	242.0 *MPa*
	S_{23}	242.0 *MPa*
B-K Power	η	1.45

Table A.2 – AS4/8552 mechanical properties

Mechanical Property	Parameter	Value
Elastic Properties	E_1	130.0 *GPa*
	E_2	9.0 *GPa*
	E_3	9.0 *GPa*
	υ_{12}	0.33
	υ_{13}	0.33
	υ_{23}	0.35
	G_{12}	5.0 *GPa*
	G_{13}	5.0 *GPa*
	G_{23}	5.0 *GPa*
Strength Properties	S_{11t}	2080.0 *MPa*
	S_{11c}	1250.0 *MPa*
	S_{22t}	75.0 *MPa*
	S_{22c}	290.0 *MPa*
	S_{12}	110.0 *MPa*
	S_{23}	110.0 *MPa*

Table A.3 – AS4/8552 intralaminar fracture toughnesses

Mechanical Property	Parameter	Value
Intralaminar Fracture Toughness	G_{1ft}	133.0×10^3 *N/m*
	G_{1fc}	40.0×10^3 *N/m*
	G_{2mt}	0.6×10^3 *N/m*
	G_{2mc}	2.1×10^3 *N/m*
	G_s	2.1×10^3 *N/m*